Micro Sun Sensor[1,2]

Carl Christian Liebe, Sohrab Mobasser, Youngsam Bae, Chris J. Wrigley, Jeffrey R. Schroeder, Ayanna M. Howard
Jet Propulsion Laboratory, California Institute of Technology
4800 Oak Grove Dr, Pasadena CA 91109-8099, USA
(818) 354 7837
firstname.lastname@jpl.nasa.gov

Abstract—A prototype micro sun sensor has been developed at the Jet Propulsion Laboratory, California Institute of Technology. It consists of a thin piece of silicon coated with a layer of chrome and a layer of gold with hundreds of small pinholes, placed on top of an Active Pixel Sensor (APS) image detector at a distance of 900 microns. Images of the sun are formed on the APS image detector when the sun illuminates the mask. Sun angles are derived by determining the precise location of the sun images on the detector – just like a sundial. The packaged micro sun sensor has a mass of 11 grams, a volume of 4.2 cm^3 and a power consumption of 30 mW. The accuracy of the micro sun sensor is better than 1 arcminute and the maximum field of view is 160°.

TABLE OF CONTENTS

1. INTRODUCTION

Sun sensors are widely used in spacecraft attitude determination subsystems to provide a measurement of the sun vector in spacecraft coordinates. Future micro/nano spacecraft and rovers will need to carry sun sensors to determine the pointing direction towards the sun or position determination. Unfortunately, conventional sun sensors are typically too large compared to the size of a micro/nano spacecraft or a small rover. Therefore, the Jet Propulsion Laboratory, California Institute of Technology has initiated an ongoing research activity to utilize Micro Electro Mechanical Systems (MEMS) processes to develop a smaller and lower mass sun sensor for space applications [1-4].

Two categories of conventional sun sensors exist - digital and analog types. The digital sun sensor illuminates different geometric patterns on the detector plane. The presence or absence of light imaged on the plane defines a digital signal that can be translated into the sun angle. In comparison, an analog sun sensor outputs analog currents, from which the sun angles can be derived directly [5]. To enhance the capabilities of these traditional sun sensor devices, a new generation of sun sensors is emerging. These sun sensors utilize an imaging device as the detector plane with a mask placed in front of it. The sun sensor determines sun angles based on the location of the image pattern on the detector plane [6-9].

The micro sun sensor is essentially a pinhole camera [10] with an F/# ~30 and multiple pinholes. It consists of two key components: 1) a MEMS based mask and 2) a "camera on a chip" APS image detector. The high-resolution multi aperture mask is placed close to the image detector. The concept is shown in Figure 1. The gray spots on the bottom plate (the focal plane) indicate the images of the sun formed by individual apertures on the top plate. The micro sun sensor utilizes a special "camera on a chip" image detector. All camera functions such as photosensitive pixels, A/D converter and control logic are implemented on the die. The sun angles in two orthogonal axes can be derived by determining the location of the sun images on the focal plane – just like a sundial.

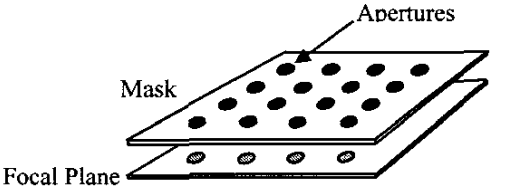

Figure 1. The micro sun sensor concept

The distance between the focal plane and the MEMS mask is approximately 900 µm and the size of the focal plane is 6.1 mm x 6.1 mm. This means that the maximum theoretical Field Of View (FOV) is ~160° (±80°). However, at larger sun angles only a few apertures is visible on the image detector and the sun images are very elongated due to internally reflections in the MEMS mask. The accuracy of the micro sun sensor decreases as a function of the sun angle.

The MEMS mask and the image detector is packaged into a small aluminum box including a connector. The image

0-7803-7231-X/01/$10.00/©2002 IEEE
[2] IEEEAC paper #274, Updated November 27, 2001

detector die is mounted directly to a PCB using "chip on board" technology. The assembly is show in Figure 2 and the specifications are shown in Table 1. This paper will describe the mask design, the APS image detector, the algorithms and the calibration of the sensor. Also, future directions for this task are discussed.

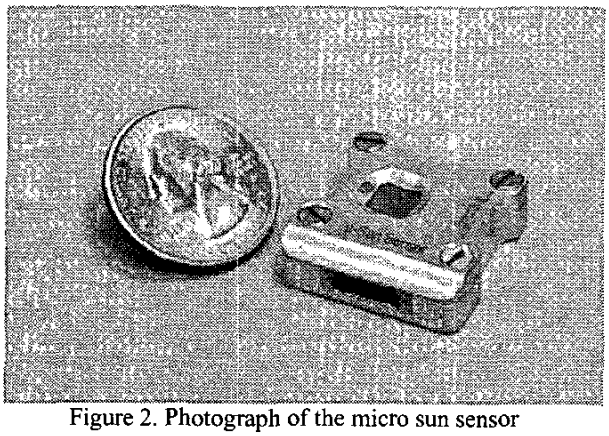

Figure 2. Photograph of the micro sun sensor

Table 1. Micro sun sensor specifications

Mass	11 grams
Power consumption	30 mW
Accuracy (1s, 1 axis)	<1 arcminute
FOV	160°
Volume	4.2 cm^3

2. MEMS MASK

To fabricate masks with hundreds of closely aligned micro size pinholes, MEMS fabrication techniques are required because the MEMS lithography-technique has extremely high precision and is well controlled. Also, MEMS technology allows the production of more than 100 masks simultaneously.

A typical MEMS mask is shown in Figure 3. Each pinhole mask is a 7mm x 7mm square. Six combinations of masks having pinhole sizes of 16, 32, and 64 μm and center-to-center spacing of 128 and 256 μm were laid out on a 10 cm diameter and 500-μm thick silicon wafer.

Figure 4 describes the fabrication steps for a MEMS pinhole mask. The bare wafer was double-side polished and 500 μm thick (Figure 4, Step 1). 590 Angstroms of chrome and 2000 Angstroms of gold were deposited with an e-beam evaporator [11, p.97]. The chrome layer was evaporated first on the wafer. The chrome layer serves two purposes: primarily as an adhesive layer since gold cannot adhere to a silicon wafer directly and secondly to attenuate the optical transmission of light through the wafer. A 2000 Angstrom gold film coating was deposited immediately after the chrome layer (Figure 4, Step 2). The next steps, steps 3 to 5 in Figure 4, resemble a printing process. A 2-μm thin photoresist (PR) was spin-deposited, and the pinhole pattern was lithographed. PR is an UV light sensitive polymer; when exposed under UV light it changes its state to be etch-*able* in a developer.

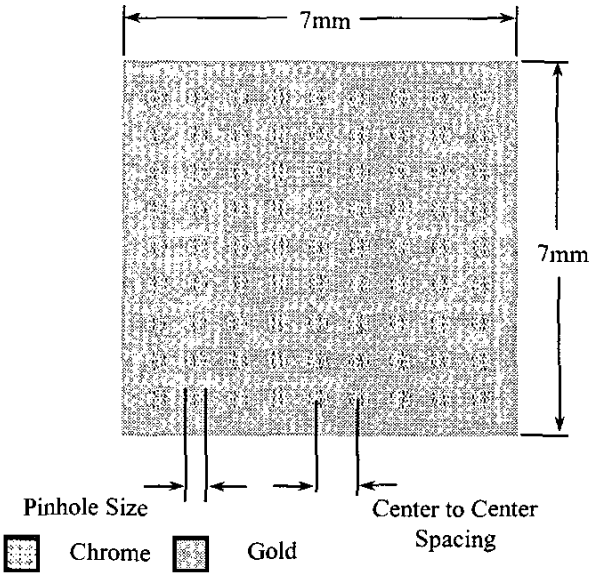

Figure 3. The MEMS pinhole mask layout

The PR coated wafer was masked with the pinhole pattern and exposed to UV light. The UV exposed area was then developed [11, p. 1-32]. At this point, the PR has pinhole-openings, exposing the thin gold metal. In next step, the wafer was put in an oxygen rich Reactive Ion Etcher (RIE) to make the patterned surface hydrophilic (attract water) (Figure 4, Step 6). Then, the wafer was dipped in a gold etchant bath. The etchant etched the gold metal where it was exposed by the photoresist openings (Figure 4, Step 7). Finally, the photoresist was stripped and the wafer diced into 7mm x 7mm dies.

Figure 5a depicts a MEMS mask with 64-μm diameter pinholes and 256-μm spacing. Figure 5b shows top and cross-section views of a 16-μm diameter pinhole; note the undercut after the thin gold metal etching step. The smaller circle is the edge of the PR opening and the 3 or 4-μm offset from the PR edge or the blurred outer circle is where gold etching stopped. The undercut takes place because the aqueous gold etchant etches isotropically.

Figure 6 is a photograph of a finished MEMS mask showing both sides of the mask. The sunlight is transmitted though the 500-μm silicon wafer and the pinholes and impinge on the APS chip. Silicon is optically transparent at wavelengths longer than ~1 μm where the APS chip is sensitive. Therefore, the silicon wafer does not provide sufficient attenuation of the sunlight. Thus, the chrome layers secondary function is to attenuate the sunlight. This will be the topic of the next paragraph.

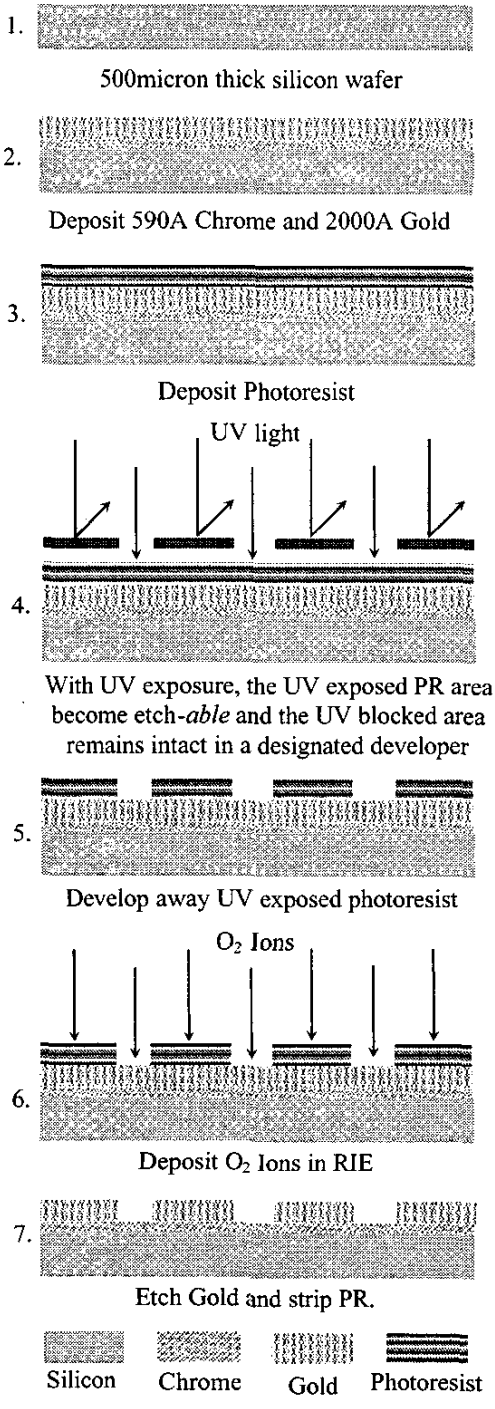

Figure 4. Cross sections of MEMS pinhole mask fabrication steps

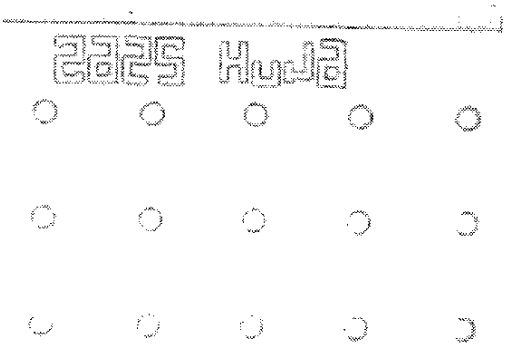

Figure 5a. A picture of a MEMS mask

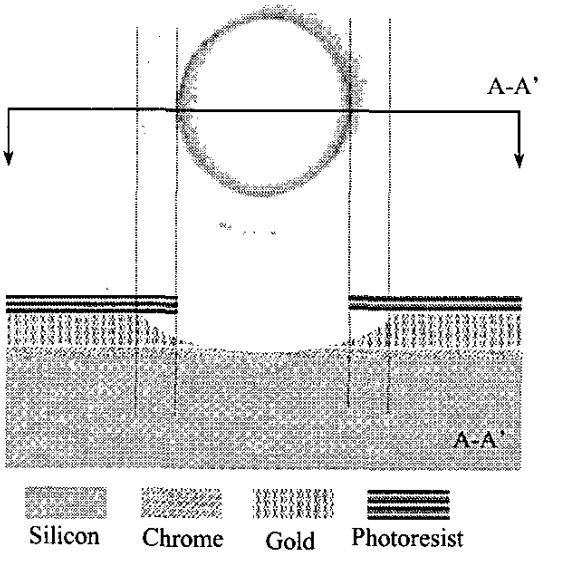

Figure 5b. A picture of a gold undercut pinhole

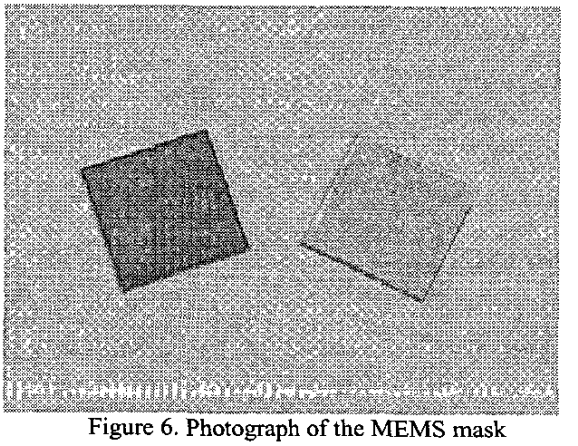

Figure 6. Photograph of the MEMS mask

The Sun is a black body radiator with a surface temperature of ~5800K. The power density in Earth orbit is ~1400 W/m^2. The size of a pixel on the APS image detector is 12 μm x 12 μm. Therefore, 189 nW is incident on an area the size of a pixel. The relative spectral distribution of the energy is shown in Figure 7. A 500-μm silicon wafer is placed in front of the pixel. The spectral transmission of the Si wafer is shown in Figure 8 [12]. The incident number of photons on a pixel behind the silicon mask can be calculated based on the total power, Figure 7 and Figure 8. The result is shown in Figure 9. The quantum efficiency of the detector (defined as the ratio of photoelectrons to the incident photons) is given in Figure 10 for the APS chip. Multiplying Figure 9 and Figure 10 will determine how many photoelectrons are detected at different wavelengths. This is shown in Figure 11. It is observed that the micro sun sensor is only sensitive in the 1.0 – 1.1 μm spectral band.

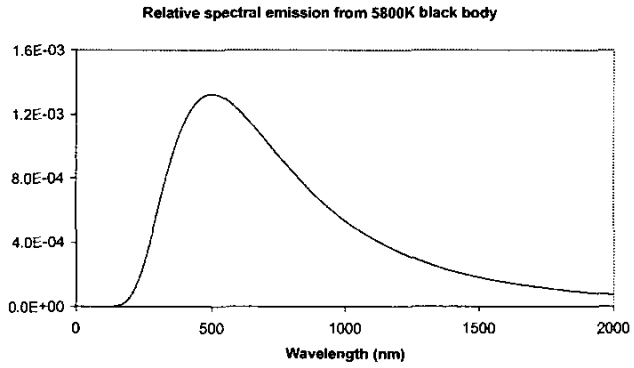

Figure 7. Relative spectral distribution of sun energy

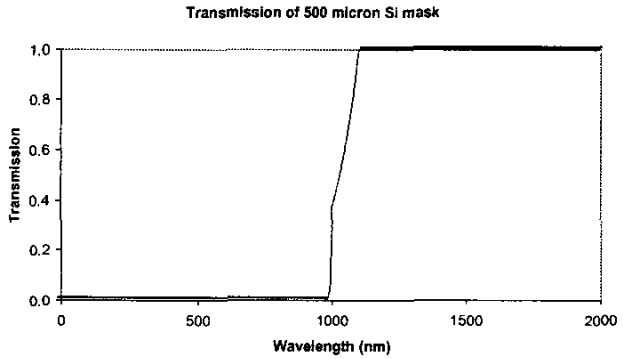

Figure 8. Spectral transmission in 500-μm Si wafer

Figure 11 shows that the total number of detected photoelectrons is $3.6 \cdot 10^8$ per pixel per second. The full well of a pixel is 240,000 photoelectrons. Since it is undesirable to reach the full well of a pixel, a sun signal of 150,000 photoelectrons was desired. It was chosen to operate the micro sun sensor with an exposure time of 100 milliseconds. Therefore the solar flux must be attenuated 240 times. The chrome layer on the silicon wafer does this. It was assumed that a 75-Angstrom thick chrome

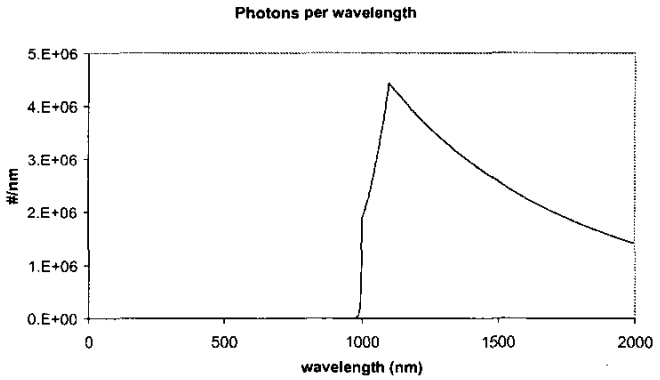

Figure 9. Number of photons incident on a pixel behind the Si mask

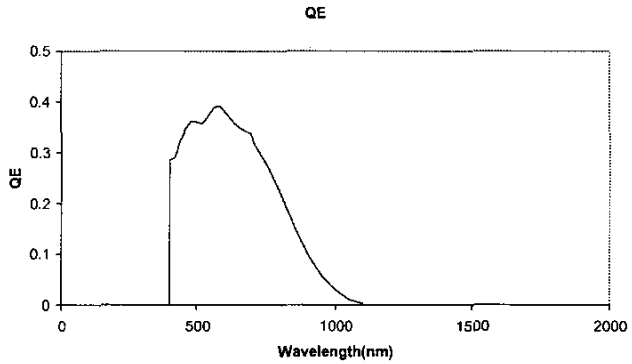

Figure 10. Quantum efficiency of the APS chip

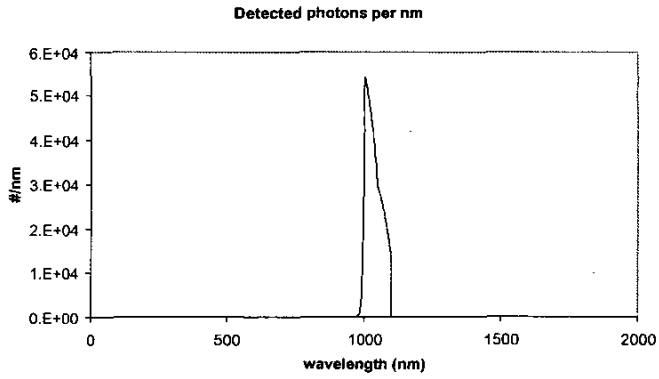

Figure 11. Detected photoelectrons at different wavelengths

layer would transmit 50% of the light [13]. 240 times is equal to $2^{7.9}$. Therefore it was decided to make the chrome layer 75 * 7.9 = ~590 Angstrom.

For the gold layer, it was assumed that a thickness of 2000 Angstrom would be completely opaque.

3 APS DETECTOR

The Versatile Integrated Digital Imager (VIDI) 512 is a complete CMOS imaging system on a chip [14]. The VIDI contains a 512 x 512 imaging array, 512 A/D converters (one for each column), D/A converters that control the internal reference voltages, currents, and a digital control block. The minimum VIDI interface consists of 5 wires: V_{dd}, Ground, Serial Data Input, Serial Data Output, and Clock. The imager configuration is programmed through the serial input port. Configuration registers are written to the serial input port either asynchronously or with an SPI (Serial Peripheral Interface) compatible synchronous protocol. All of the configuration registers are double buffered; registers written during imaging do not take effect until that image is completed. The configuration determines the pixel timing and ADC signals that are generated internally. After the imager is configured, a single command through the serial input port will cause image data to be taken. The images can be output in the form of serial or parallel data or with a pair of differential analog voltages. The image serial output is SPI compatible to ease interface compatibility between the VIDI and external data collection hardware. There is a power down mode that shuts down all the internal circuitry except for the serial input port so power consumption can be minimized when the camera is not in use. The imager can be programmed to perform an internal column voltage offset correction to minimize column fixed pattern noise. A block diagram of the VIDI is shown in Figure 12.

The imager is a 512 by 512 photodiode pixel array. It can randomly access any window in the array, from 1 pixel x 1 pixel all the way to 512 pixels x 512 pixels in any rectangular shape. Integration can be set as low as one row read time to $2.1 \cdot 10^9$ row times. The window size and integration time are set with configuration registers.

The VIDI512 is configured by writing values to internal registers through the serial input port. The port can be written to at any time. Serial input words that are written during an imaging operation take effect at the end of the current image frame. While the VIDI is imaging the first picture, the serial port can accept commands to configure the second picture. When the first picture is complete, the second picture can be taken immediately. There is no delay to configure the VIDI.

An offset correction algorithm in the VIDI minimizes any column fixed pattern noise. With zero signal, the difference between the reset and signal levels is measured for each column output ADC circuit. This difference is

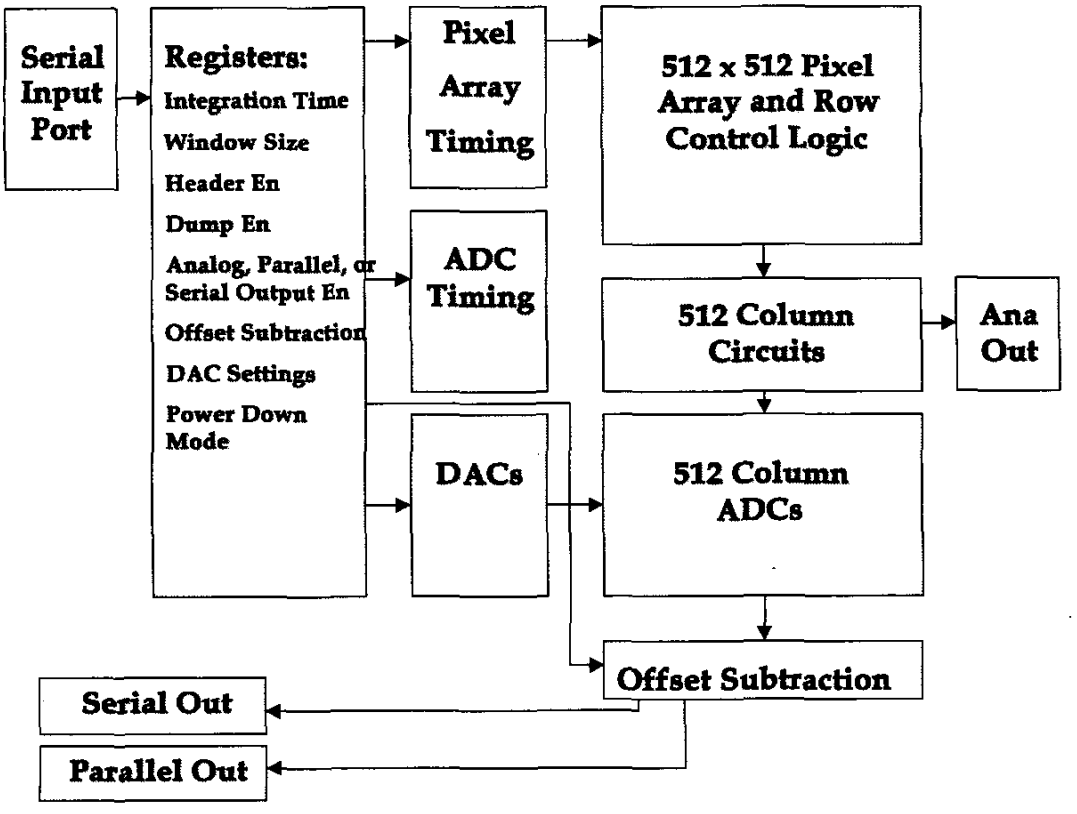

Figure 12. VIDI Block Diagram

digitally subtracted from each row's data when the OSE (Offset Subtraction Enable) bit in the Control Register is set high. The offset data row is output whether or not the Offset Subtraction is enabled. A summary of the VIDI specifications is given in Table 2.

Table 2. VIDI Specifications and summary of measured values

Characteristics	Values
Technology	CMOS, 0.5μm
Outputs	Analog & Digital
Format	512 x 512
Pixel Size	12 μm x 12 μm
Responsivity	4 μV/photon
Quantum efficiency	42% (peak @ 550 nm)
Dark Current	300 pA/cm^2
Noise	40 e$^-$
ADC resolution	10 bits (9.3 bits effective)
Power	10 mW @ 30 FPS

4 ALGORITHMS

In an image captured from the micro sun sensor, a pattern of approximately 300 equally spaced apertures is typically observed as shown in Figure 13. The position of this pattern on the focal plane changes as a function of sun angle. In order to calculate the sun angles, the positions of the aperture centroids on the focal plane have to be determined. This type of image processing is routinely done in star trackers [15-16], where the centroids of bright spots (stars) are found in an image. The image is sifted for pixels that are above a given threshold. Once such a pixel is detected, a region of interest (ROI) window is aligned with the detected pixel in the center. The average pixel value on the border is calculated as shown in Figure 14 and subtracted from all pixels in the ROI.

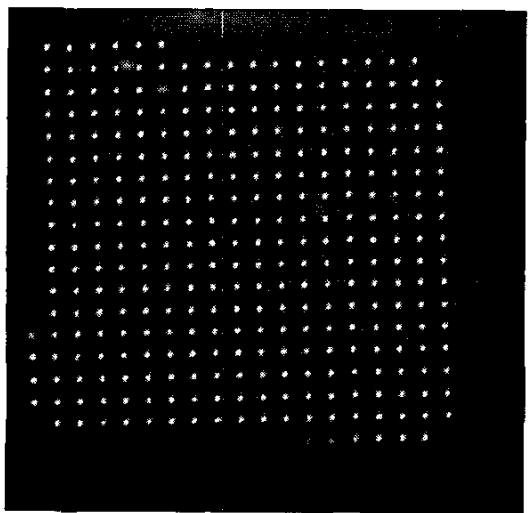

Figure 13. Typical image acquired with the micro sun sensor. The partially illuminated apertures at the rim of the image are just an artifact of the setup

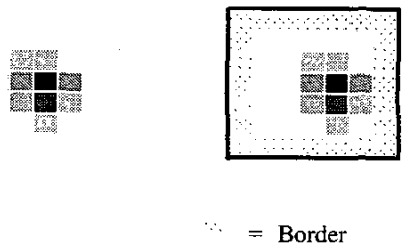

Figure 14. The region of interest (ROI), and the border of the ROI of a detected bright spot

The brightness in units of A/D converter numbers (DN) and the centroid (x_{cm}, y_{cm}) are calculated from the background-subtracted pixels in the ROI.

$$DN = \sum_{i=ROIstart,i}^{ROIend,i} \sum_{j=ROIstart,j}^{ROIend,j} image(i,j) \quad (1)$$

$$x_{cm} = \sum_{i=ROIstart,i}^{ROIend,i} \sum_{j=ROIstart,j}^{ROIend,j} \frac{i \cdot image(i,j)}{DN} \quad (2)$$

$$y_{cm} = \sum_{i=ROIstart,i}^{ROIend,i} \sum_{j=ROIstart,j}^{ROIend,j} \frac{j \cdot image(i,j)}{DN} \quad (3)$$

Figure 15 shows the positions of all the identified ROIs from the image shown in Figure 13.

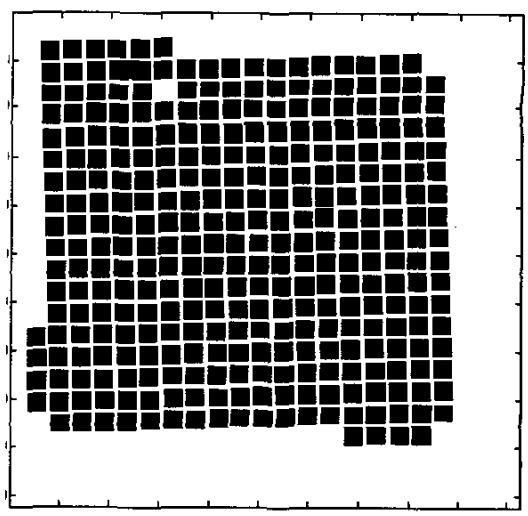

Figure 15. The position of all ROIs in the image in Figure 13

The resulting centroids are shown in Figure 16. The centroids are shown with red +'s. Note that one aperture is not bright enough to be detected.

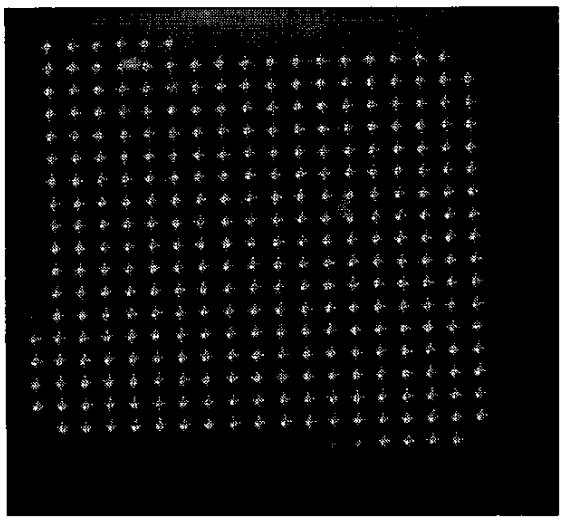

Figure 16. The identified bright spots from Figure 13 are identified with red +'s

5. HELIOSTAT TESTING

JPL's Celestial Simulator facility was used to test the micro sun sensor. The facility contains a Heliostat, which is simply a "sun tracker". The heliostat consists of a large mirror mounted on a two-axis gimbal inside a dome attached to the facility. The sun is tracked using this gimbal system and the sun bundle is directed toward a fixed mirror located on the ceiling of the facility. The end result of all this is that there is a 3 foot diameter sun "bundle" in the middle of the room inside the facility for about 4-6 hours around noon time (depending on the season). A picture of the heliostat is shown in Figure 17.

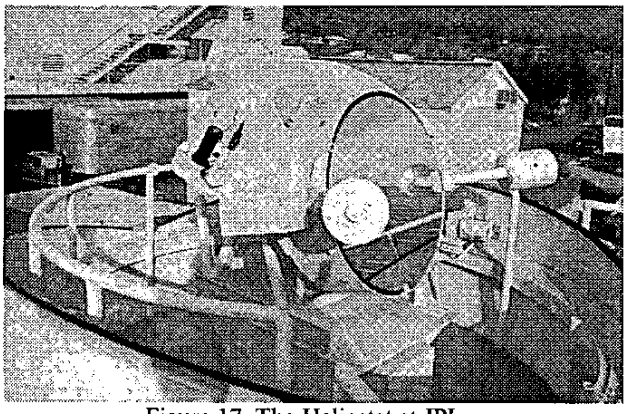

Figure 17. The Heliostat at JPL

A 2-axis gimbal holding the micro sun sensor is rotated though a large number of different angles and the aperture centroids are recorded. Based on all these measurements, it is possible to derive the relationship between the centroids and the sun angles. A sketch of the 2-axis gimbal with the micro sun sensor is shown in Figure 18. The dashed lines indicate the two axes of rotation.

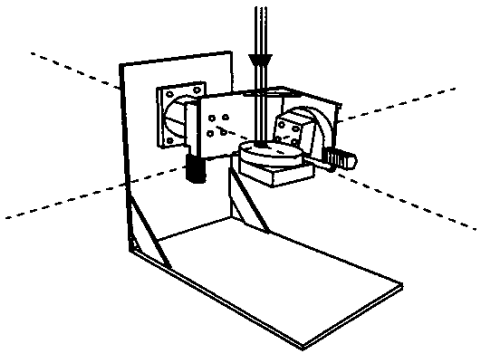

Figure 18. A sketch of the 2-axis gimbal used to calibrate the micro sun sensor

6. SENSOR MODEL

The sensor model is a mathematical equation that relates centroid coordinates to the orientation of the sun in an instrument based coordinate system.

Only a single aperture centroid has been calibrated and characterized in this section. The described procedure is applied to multiple apertures in the next section. The single aperture that was evaluated was chosen randomly and is shown in Figure 19 with a red +.

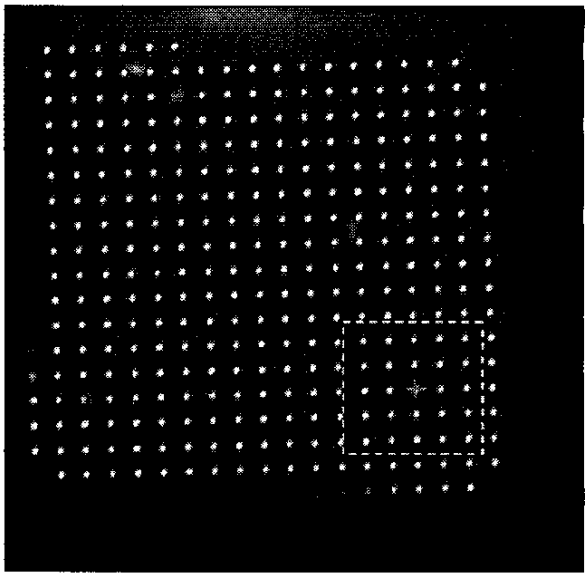

Figure 19. The single aperture that is characterized in this paper is indicated with a red +

The gimbal was slewed from –32° to +28° in steps of 4° in one axis and from –40° to +40° in steps of 4° in the other axis. There were a total of 336 images acquired at different orientations. Since one gimbal axis is located on the other gimbal axis, the pattern that the aperture will

sweep over on the focal plane is not symmetric. Figure 20 depicts the positions of the red aperture in Figure 19 over the 336 images.

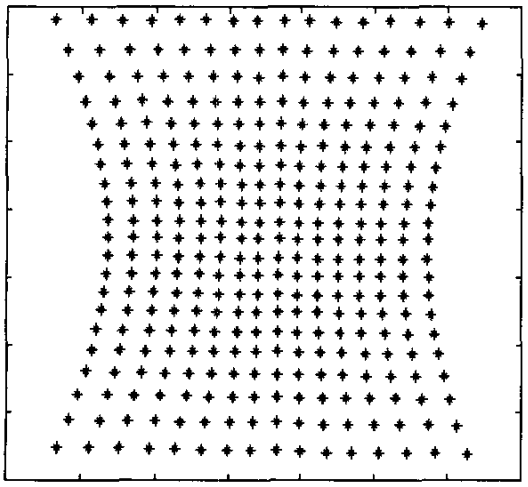

Figure 20. The position of the aperture centroid on the focal plane. The size of Figure 20 is shown with a green dashed line in Figure 19

The sensor model is a simple pinhole camera model. The pinhole model consists of 6 parameters: the focal length (F), the intersection of boresight with the focal plane (x_0, y0), and the rotation from the focal plane coordinate system to the external coordinate system (3 different Euler angles, a, ß, f). It can be shown that the equations for mapping from gimbal angles to centroid coordinates are [2]:

$$\begin{pmatrix} x \\ y \end{pmatrix} = \begin{pmatrix} F \cdot \frac{\tan(\beta - \beta_0)}{\cos(\alpha - \alpha_0)} \cdot \cos\phi - F \cdot \tan(\alpha - \alpha_0) \cdot \sin\phi - x_0 \\ -F \cdot \frac{\tan(\beta - \beta_0)}{\cos(\alpha - \alpha_0)} \cdot \sin\phi - F \cdot \tan(\alpha - \alpha_0) \cdot \cos\phi - y_0 \end{pmatrix} \quad (4)$$

During the data acquisition, 336 measurements were collected. This vector set of angles is called a and ß. For each measurement, a set of observed (x, y) centroids on the focal plane was also observed. The four vectors are:

$$\overline{\alpha} = \begin{pmatrix} \alpha_1 \\ \alpha_2 \\ \cdot \\ \alpha_{336} \end{pmatrix} \quad \overline{\beta} = \begin{pmatrix} \beta_1 \\ \beta_2 \\ \cdot \\ \beta_{336} \end{pmatrix} \quad \overline{x_m} = \begin{pmatrix} x_{m,1} \\ x_{m,2} \\ \cdot \\ x_{m,336} \end{pmatrix} \quad \overline{y_m} = \begin{pmatrix} y_{m,1} \\ y_{m,2} \\ \cdot \\ y_{m,336} \end{pmatrix} \quad (5)$$

There are only 6 unknowns. They are a_0, $ß_0$, f , x_0, y_0 and F. We want to find a solution that minimizes the squared distance between the calculated and measured aperture centroids. Therefore, we want to minimize the following equation (6):

$$\sum_{i=1}^{336} \left(F \frac{\tan(\beta_i - \beta_0)}{\cos(\alpha_i - \alpha_0)} \cos\phi - F \tan(\alpha_i - \alpha_0) \sin\phi - x_0 - x_{m,i}\right)^2 + \left(-F \frac{\tan(\beta_i - \beta_0)}{\cos(\alpha_i - \alpha_0)} \sin\phi - F \tan(\alpha_i - \alpha_0) \cos\phi - y_0 - y_{m,i}\right)^2 \quad (6)$$

This can be solved utilizing Matlab or the Solver in Excel.

The following optimal parameters were found:

$$\begin{aligned} x_0 &= 352.08 \quad F = 907.7\mu \quad \alpha_0 = -1.25° \\ y_0 &= 369.54 \quad \phi = 0.808° \quad \beta_0 = 1.26° \end{aligned} \quad (7)$$

The average error for the solution was found to be 0.173 pixels (0.13°). The average error is the average distance between the measurements and the sensor model (8).

$$\frac{1}{336} \sum_{i=1}^{336} \sqrt{\left(F \frac{\tan(\beta_i - \beta_0)}{\cos(\alpha_i - \alpha_0)} \cos\phi - F \tan(\alpha_i - \alpha_0) \sin\phi - x_0 - x_{m,i}\right)^2 + \left(-F \frac{\tan(\beta_i - \beta_0)}{\cos(\alpha_i - \alpha_0)} \sin\phi - F \tan(\alpha_i - \alpha_0) \cos\phi - y_0 - y_{m,i}\right)^2} \quad (8)$$

7. MULTIPLE APETURES

In the previous section the calibration and characterization of a single aperture was explored. However, the mask consists of hundreds of apertures and the potential of using multiple apertures simultaneous to increase the accuracy is investigated in this section.

For this investigation 10 apertures were chosen randomly. The 10 random apertures are shown with red + in Figure 21. The calibration procedure described in Section 6 was applied to each aperture individually.

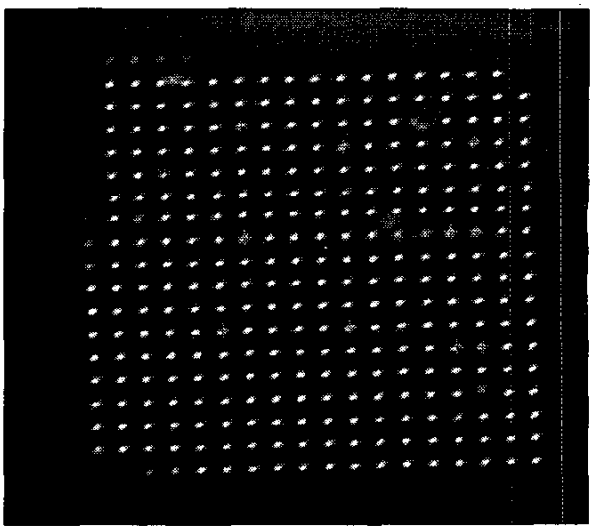

Figure 21. Ten randomly chosen apertures

The residual angular error for each of the 10 apertures were calculated for all 336 images and plotted in the same graph. This is shown in Figure 22.

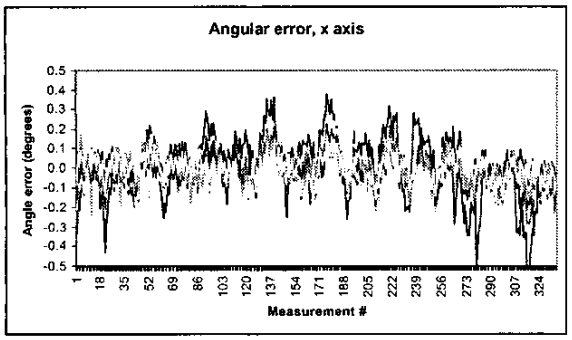

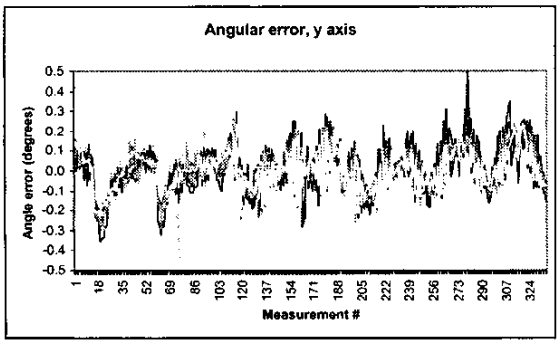

Figure 22. The residual x and y angular error for the 10 apertures. The average accuracy for a single aperture is 0.1°

It is observed that there is a very strong correlation between the 10 individual apertures. This indicates that the apertures are not independent and some external perturbation is applied to the whole micro sun sensor. An investigation showed that both the heliostat and the 2-axis gimbal were not accurate down to the sub arcminute level. It is therefore concluded that the majority of the single aperture accuracy of 0.1° is caused by errors in the test setup and the accuracy of the micro sun sensor itself is much better.

To assess the error of the micro sun sensor itself, the average angular error of the 10 apertures was calculated for each of the 336 measurements. This angle was assumed to represent the test setup perturbation. This angle was then subtracted from the individual measurements. The result is shown in Figure 23.

In Figure 23 it is observed that the accuracy of a single aperture is ~0.04°. When common errors have been removed, it is possible to combine the different aperture measurements and increase the accuracy with the square root of the number of apertures. In theory, using 100 apertures should increase the accuracy by a factor of 10 to 0.004°. However, this requires that the apertures are completely independent. Therefore, it is conservatively estimated that the accuracy of the micro sun sensor is better than 1 arcminute.

8. FUTURE DIRECTION OF THE PROJECT

Dynamic range is an issue for all sun sensors flying on interplanetary missions. As an example, a mission doing a gravity-assist swingby of Venus on the way to Pluto must be able to track the sun from 0.72AU to 40 AU. The brightness of the sun changes more than a factor of 3000 and the angular size of the sun changes from 0.7° to 0.01°. Such huge intensity difference is a problem to most sun sensors. Adjusting the exposure time of the sun sensor cannot compensate for this intensity difference. Therefore, it is proposed that there are a number (e.g. 4) of different thicknesses of chrome in the different pinholes. In this way, some pinholes would be optimized to image the Sun at Venus and other pinholes would be optimized to image the Sun at Pluto. The "Venus" pinholes would be dark at Pluto and the "Pluto" pinholes would be saturated at Venus. Fortunately, an APS chip does not bloom like a CCD chip. Changes of the angular size of the sun will not affect the design.

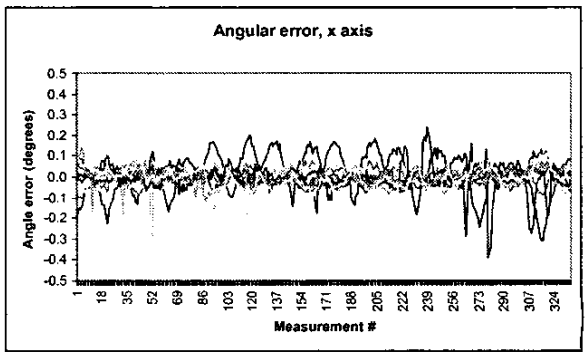

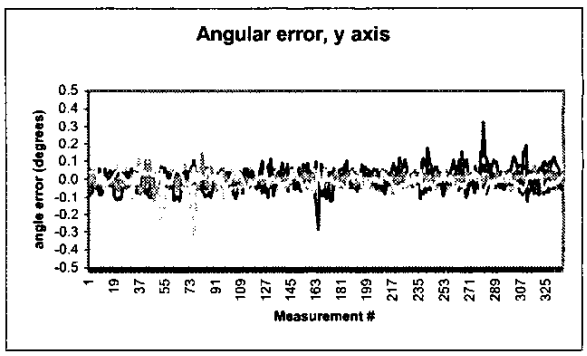

Figure 23. The residual x and y angular error for the 10 apertures. The test setup perturbations have been subtracted. The average accuracy for a single aperture is 0.04°

In the proposed system, the spacecraft computer does the centroiding. This is processor intensive. Basically, the computer has to read all pixels. It then has to compare all pixels to a threshold value. When a bright pixel is detected, it has to calculate the centroid. In Matlab, a non-optimized program takes approximately 1 million instructions to do this on an image. Utilizing a priori knowledge of the centroid positions can reduce the

required processor load substantially, but still the entire image has to be loaded for each attitude update. Therefore another possibility should be explored. On APS chips, it is possible to place additional logic on the focal plane. Experiments have been done to place the centroid calculation function on the chip itself [17]. This means that the APS chip would only output centroids. This would take a large burden off the spacecraft computer.

9. SUMMARY

A new type of sun sensor based on MEMS technology has been described in this paper. A tiny gold and chrome plated silicon wafer is placed at a distance of 900 microns from an APS chip. The APS chip contains all camera functions on the chip. The mask consists of hundreds of pinholes. The sun angle can be determined based on the position of the aperture centroids – just like a sundial.

The centroid of the apertures is calculated with algorithms similar to those utilized in star trackers. Calibrations show that the accuracy is better than 1 arcminute utilizing multiple apertures.

The MEMS mask and the focal plane has been packaged together. The mass of the micro sun sensor is 11 grams. This miniaturization represents more than an order of magnitude improvement over current state-of-the-art sun sensors.

ACKNOWLEDGEMENTS

The research described here was carried out at the Jet Propulsion Laboratory, California Institute of Technology, under a contract with the National Aeronautics and Space Administration. References herein to any specific commercial product, process or service by trademark, manufacturer, or otherwise, does not constitute or imply its endorsement by the United States Government or the Jet Propulsion Laboratory, California Institute of Technology.

REFERENCES

[1] Ian Sample: Space-age sundials help satellites look on the bright side, New Scientist, 21 April 2001, No. 2287, page 20.

[2] C.C.Liebe, S. Mobasser: MEMS based sunsensor, Aerospace Conference, 2001, IEEE Proceedings. Volume: 3, 2001, Page(s): 1565 –1572.

[3] S.Mobasser, C.C.Liebe, A.Howard: Application of Fuzzy Logic in Sunsensor Data Interpretation, to appear in the proceedings of The Second International Conference on Intelligent Technologies (InTech'2001), Bangkok, Thailand, November 27-29, 2001.

[4] S.Mobasser, C.C.Liebe, A.Howard: Fuzzy Image Processing in Sun Sensor, to appear in proceedings of 10th IEEE International Conference on Fuzzy Systems, Dec. 2-5 2001, Melbourne, Australia.

[5] James R. Wertz: Spacecraft Attitude Determination and Control, D.Reidel Publishing Company, Dordrecht, Holland.

[6] TNO TPD, Netherlands: http://www.tpd.tno.nl/TPD/smartsite88.html cited September 6th 2001.

[7] Ninomiya, Keiken; Ogawara, Yoshiaki; Tsuno, Katsuhiko; Akabane, Satoshi: High accuracy sun sensor using CCDs, AIAA Guidance, Navigation and Control Conference, Minneapolis, MN, Aug. 15-17, 1988, Technical Papers. Part 2 (A88-50160 21-08). Washington, DC, American Institute of Aeronautics and Astronautics, 1988, p.1061-1070.

[8] Kouzmin, Vladimir S; Cheremoukhin, Gennadi S; Fedoseev, Victor I: Miniature sun sensor, SPIE Proceedings. Vol. 2739, 1996, p. 407-410.

[9] Lockheed Missiles & Space Company, Sunnyvale, CA: Sun Sensors, Fact Sheet, 1985.

[10] Eugene Hecht: Optics, Addison-Wesley Pub Co; ISBN: 0201838877.

[11] Madou, M. (1997) Fundamentals of Micro fabrication, New York: CRC Press.

[12] Donald Rapp: Thermo-Optical Properties of Silicon, Jet Propulsion Laboratory, California Institute of Technology, Pasadena, CA 91109, http://www.gps.caltech.edu/genesis/Thermal-Coll.html, Cited: 9/4/2001.

[13] O.S.Heavens: Optical Properties of thin solid films, Dover Pubns; ISBN: 0486669246.

[14] B.Pain et al: A Single-chip Programmable digital CMOS Imager with Enhanced Low-light Detection Capability, Proc. 13th VLSI design Conference, Calcutta, India, January 2000, pp. 342-347.

[15] Liebe, Carl C; Dennison, Edwin W; Hancock, Bruce; Stirbl, Robert C; Pain, Bedabrata: Active Pixel Sensor (APS) based star tracker, 1998 IEEE Aerospace Conference, Aspen, CO, Mar. 21-28, 1998, Proceedings. Vol. 1 (A98-34386 09-31), p. 119-127.

[16] C.C.Liebe: Star Trackers for Attitude Determination, IEEE AES Magazine June 1995, p.10-16.

[17] G. Sun, G.Yang, O.Yadid-Pecht and B.Pain: A smart CMOS Imager with On-chip High-speed Windowed

Centroiding Capability, 1999 IEEE Workshop on charge coupled devices and advanced image sensors, Nagano, Japan, pp. 66-71, June 10-12, 1999.

Dr. **Carl Christian Liebe** received the M.S.E.E. degree in 1991 and the Ph.D. degree in 1994 from the Department of Electrophysics, Technical University of Denmark. Since 1997 Dr. Liebe has been with the Jet Propulsion Laboratory, California Institute of Technology. Currently, he is a senior member of the technical staff in the Precision Motion Control Systems & Celestial Sensors Group. He has more than 10 years of experience in star trackers, sun sensors, target tracking and image processing. His current research interests include miniaturization of attitude determination sensors. He has authored/co-authored more than 40 papers.

Dr. **Sohrab Mobasser** received his Ph.D. from Stevens Institute of Technology at New Jersey in experimental solid-state physics in 1982. He is a Senior Member of the Engineering Staff at the Jet Propulsion Laboratory, California Institute of Technology. Sohrab has more than 18 years of aerospace industry experience, most of it in spacecraft attitude determination. His work can be found on many planetary missions, from the Galileo mission to Jupiter to the successful Pathfinder mission to Mars and the Cassini mission to Saturn. His current interests are new technology and applications for autonomous attitude determination.

Sam Y. Bae received his master's degree in mechanical engineering at Purdue University and bachelor's degree in Engineering Physics at UC Berkeley. He has been a Member of the Technical Staff at Jet Propulsion Lab's Micro Device Lab since 1997. He has been involved with thick film lithography, miniature scroll pump; MEMS based micro-gyroscope, and the current work, Sun Sensor.

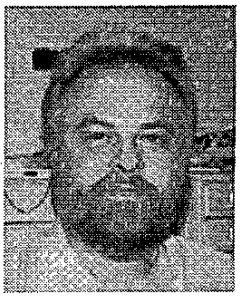

Chris J. Wrigley received his MSEE and BSEE from California State University of L.A. in Electrical Engineering in 1998 and 1996 respectively. He is currently a Member of the Technical Staff in the Advanced Imager and Focal Plane Technology group as the lead Test and Characterization engineer. Chris joined JPL as Instrumentation Specialist in 1987 and later joined his current group in 1997. He has 21 years of experience spanning many disciplines including power, communications, computers, instrumentation, and electronics. His current interests are new technology and applications utilizing Active Pixel Sensors (APS) focal planes.

Jeff Schroeder is a Senior Technical Assistant who has worked at JPL for 22 years. He specializes in mechanical design and fabrication, and has worked on many flight and development projects. His interest in astronomy includes 25 years as a planetarium lecturer, construction of an 11" refracting telescope, and eclipse chasing around the world. The recently upgraded 48" Palomar Schmidt telescope uses a CCD camera that he designed and built for the Near Earth Asteroid Tracking (NEAT) program. For this and earlier work on the program, asteroid 19290 Schroeder was named this year. Presently, in his spare time, he is working on his second homebuilt airplane.

Dr. **Ayanna Howard** received her M.S.E.E. degree in 1994 and Ph.D. in Electrical Engineering in 1999 from the University of Southern California, Los Angeles. Since 1993, she has been at the NASA-Jet Propulsion Laboratory, California Institute of Technology where she has led research efforts on various projects utilizing vision, fuzzy logic, and neural network techniques. Dr. Howard currently serves as Member of Technical Staff in the Telerobotics Research and Applications Group where her main emphasis is focused on utilizing artificial intelligence algorithms for real-time autonomous systems.

This page intentionally left blank.